NASA Technical Paper 3039

August 1990

Spent-Beam Refocusing Analysis and Multistage Depressed Collector Design for a 75-W, 59- to 64-GHz Coupled-Cavity Traveling-Wave Tube

Jeffrey D. Wilson,
Peter Ramins,
and Dale A. Force

NASA

NASA Technical Paper 3039

1990

Spent-Beam Refocusing Analysis and Multistage Depressed Collector Design for a 75-W, 59- to 64-GHz Coupled-Cavity Traveling-Wave Tube

Jeffrey D. Wilson,
Peter Ramins,
and Dale A. Force
Lewis Research Center
Cleveland, Ohio

National Aeronautics and Space Administration
Office of Management
Scientific and Technical Information Division

Trade names or manufacturers' names are used in this report for identification only. This usage does not constitute an official endorsement, either expressed or implied, by the National Aeronautics and Space Administration.

Summary

A computational design technique for coupled-cavity traveling-wave tubes (TWT's) equipped with spent-beam refocusers (SBR's) and multistage depressed collectors (MDC's) is described. A large-signal multidimensional computer program was used to analyze the TWT–SBR performance and to generate the spent-beam models used for MDC design. The results of a design involving a 75-W, 59- to 64-GHz TWT are presented. The SBR and MDC designs are shown, and the computed TWT, SBR, and MDC performances are described. Collector efficiencies in excess of 94 percent led to projected overall TWT efficiencies in the 40-percent range.

Introduction

This report describes a newly developed computational procedure to design coupled-cavity traveling-wave tubes (TWT's) equipped with spent-beam refocusers (SBR's) and multistage depressed collectors (MDC's); it also presents the computational results of a design involving a 75-W, 59- to 64-GHz TWT. The design procedure closely parallels that devised for helical TWT's and klystrons (refs. 1 and 2). NASA Lewis Research Center's multidimensional, coupled-cavity TWT computer model (refs. 3 and 4) was used to simulate both the TWT and the SBR. The MDC was designed and its performance analyzed with the steady-state Herrmannsfeldt Electron Trajectory Program (ref. 5).

This new computational procedure was used to design an SBR and two four-stage, isotropic-graphite-electrode MDC's for a dual-mode (75- and 30-W), 59- to 64-GHz TWT being developed by Hughes Aircraft Company under NASA Contract NAS3–25090. This TWT, Model 961HA, is a modified version of the Hughes 961H, which was developed previously for NASA (ref. 6). The two experimental TWT's that will be fabricated and evaluated under the contract will incorporate these SBR and MDC designs.

The Hughes TWT Model 961HA is intended to be a space qualifiable laboratory test vehicle for future intersatellite link systems. Since various RF output power levels are still under consideration by system designers, the TWT was designed to be operated at more than one saturated output power level by controlling the beam voltage and current. Nominally, the TWT is a dual-mode tube with minimum RF output power levels of 75 and 30 W in the high and low modes, respectively. The RF design was optimized for the high-power mode. The TWT employs a coupled-cavity slow-wave circuit consisting of three sections separated by severs, with a two-step velocity taper in the output section. Periodic permanent magnets (PPM's) focus the electron beam. The general characteristics of the TWT are shown in table I.

The MDC general characteristics are shown in table II. The relatively large number of collector stages and the use of low secondary-electron-emission yield electrode material were based on the need to achieve very high collector efficiencies. The MDC efficiency is critical to achieving the program goal of an overall efficiency in excess of 40 percent at midband frequency. Because of the low basic efficiency of this TWT, small improvements in collector efficiency lead to disproportionately large improvements in the overall TWT efficiency (ref. 7). The MDC was designed to be of minimum size consistent with the high operating voltages of nearly 20 kV.

In the following sections, the analytical models and computational procedures are briefly described, the SBR and MDC designs are shown, and the computed TWT–SBR–MDC performances are presented.

Symbols

a	drift tunnel radius in TWT
b	beam outer radius at RF input
E_{min}	energy of slowest ring of charge in the spent beam
I_0	beam current, dc
P_{RF}	RF output power
R	drift tunnel radius in SBR
r	beam radius
r_{max}	beam edge radius
V_{en}	potential of collector electrode n with respect to ground
V_0	potential of cathode with respect to ground

TABLE I.—GENERAL CHARACTERISTICS OF HUGHES AIRCRAFT COMPANY TWT MODEL 961HA

Characteristic	High mode (75 W)	Low mode (30 W)
Frequency, GHz	59 to 64	59 to 64
RF output power, W	75	30
RF efficiency, percent	5.2	3.5
Cathode voltage, V	19 215	19 300
Cathode current, A	0.075	0.045
Perveance, $A/(V)^{3/2}$	0.028×10^{-6}	0.017×10^{-6}

TABLE II.—GENERAL CHARACTERISTICS OF MULTISTAGE DEPRESSED COLLECTOR FOR TWT 961HA

Type	Axisymmetric, with one electrode at cathode potential
Number of depressed stages	4
Electrode material	Machined isotropic graphite
Active size	3-cm diam by 5-cm long
Cooling	Conduction to baseplate

Analytical Models

Traveling-Wave Tube

The NASA Lewis Research Center 2½-dimensional coupled-cavity TWT model (refs. 3 and 4) calculates the interaction of a 2-dimensional RF circuit field with an electron beam. At the beginning of the circuit the beam is simulated by a series of 24 disks extending over an axial distance of an RF wavelength, with each disk divided into a maximum of 4 axially symmetric rings (the innermost ring is a disk). As the rings move axially, they also rotate azimuthally and expand and contract radially, penetrating each other in both the radial and axial directions. The RF circuit fields and electric ring trajectories are determined from the calculated axial and radial space-charge, RF, and periodic-permanent-magnet (PPM) focusing forces as the rings pass through a sequence of cavities. Each cavity has independently entered geometrical and electrical parameters, thereby enabling the model to simulate severs and velocity taper designs. Relativistic and backward wave effects are included. The model does not include thermal velocity effects in the beam.

At the RF output, the computer program lists the following:

(1) RF output power
(2) RF circuit losses
(3) Sever and attenuator losses
(4) Intercepted current and power
(5) Centroid radius of each ring
(6) Three velocity components of each ring
(7) Relative phase of each ring

Spent-Beam Refocuser

At the RF output, the electron beam enters the SBR, a short transition tunnel with PPM focusing. The purposes of the SBR are to make room for the output circuit assembly, to provide spatial isolation between the RF output and any backstreaming current from the MDC, and, possibly, to improve the MDC efficiency by debunching and reconditioning the spent beam.

The same computer model that simulated the TWT slow-wave circuit was used for the SBR. The model was modified to permit the computation of the electron beam flow in a region where the tunnel diameter changes discontinuously. This modification permits the analysis of a wide variety of possible SBR configurations.

Multistage Depressed Collector

After passing through the SBR, the spent beam enters the MDC, where the electron ring trajectories are treated as continuous rays of current; that is to say, complete debunching is assumed. Each current ray is located at the centroid of charge of its corresponding ring and has the velocity of the ring centroid. The trajectory calculation is continued until the current rays strike the MDC electrodes. The effect of secondary-electron emission from electrode surfaces is analyzed by injecting reduced charges at the points of impact of the primary current rays and tracking their trajectories to their final termination within the MDC or TWT. The effects of further secondary-electron emission due to these secondaries are neglected. Based on the final location of the primary and secondary charges, a calculation is made of the collected current, recovered power, and dissipated power at each of the collector electrodes and, if backstreaming occurs, at the TWT itself. These results, when coupled with the outputs of the TWT computer program, provide a detailed picture of the current and power flow within the TWT-SBR-MDC system.

Analytical Procedure

The computational design procedure was used to produce a slightly different MDC design for each of the two identical Model 961HA TWT's to be fabricated under Contract NAS3-25090. This was necessary because the first design had to be finished and delivered to Hughes Aircraft before the modifications to the TWT computer program that permitted step changes in the tunnel radius were fully implemented. Consequently, the designs were based on slightly different models for the spent electron beam; the first design was based on beam models that neglected the effects of a 50-percent expansion in the SBR tunnel radius. Several beam models (to simulate various TWT-SBR-MDC operating conditions) were used in producing each MDC design. These TWT-SBR-MDC operating conditions are shown in table III and discussed further in the following sections of this report. Each MDC was designed to perform well at all of these selected operating conditions, with a minimum of backstreaming to the TWT.

TABLE III.—TWT-SBR-MDC OPERATING CONDITIONS AND SPENT-BEAM MODELS CONSIDERED IN DESIGNING OF THE MDC

Case	TWT mode	Frequency, GHz	Beam model	MDC voltages
MDC design 1[a]				
1	High	61.5	As computed	Optimized for case1
2	High		Injection angles × 1.5	Optimized for case 1
3	High		As computed	Same as case 1 except V_{e1} reduced
4	Low		As computed	Optimized for case 4
MDC design 2[b]				
5	High	61.5	As computed	Optimized for case 5
6	High	61.5	Injection angles × 1.5	Optimized for case 5
7	High	64.0	As computed	Optimized for case 5
8	Low	61.5	As computed	Optimized for case 8

[a]Analysis neglects effects of spent-beam refocuser drift tunnel expansion.

[b]Analysis treats spent-beam refocuser drift tunnel expansion.

Traveling-Wave Tube

In general, the TWT performance and spent-beam characteristics were computed by using the nominal values of the TWT design parameters supplied by Hughes Aircraft and by using the 72-ring per RF-wavelength option to model the electron beam. There were two exceptions, however: (1) the initial beam radius and (2) the RF input power. After brief parametric studies, values that would yield negligible beam interception and saturation, respectively, were selected for these parameters. The computations were carried out for both power modes and at two operating frequencies: (1) midband, where RF output power (P_{RF}) is maximum, and (2) the high-band edge, where the slowest spent-beam electrons were expected (ref. 6). The computed values of P_{RF} were multiplied by a factor of 0.955 (based on ref. 6) to account for window losses.

Spent-Beam Refocuser

The SBR design was selected somewhat arbitrarily. A previous study involving a wide range of TWT's (ref. 8) had indicated (1) that for many TWT's equipped with small MDC's, an SBR that provides beam expansion and recollimation was not required (nor even desired), and (2) that an efficient MDC could be designed for virtually any beam, as long as the injection angles and space charge were not excessive. Consequently, the full-strength PPM stack simulation was continued beyond the RF output, and the spent-beam characteristics were examined at five successive magnetic field zeroes. A well-collimated beam with very small angles and adequate levels of space charge was observed at all points. Therefore, a relatively short SBR with three extra, full-strength permanent magnets beyond the RF output of the TWT was tentatively selected, because this configuration would be very easy to implement experimentally. The tunnel radius of the SBR was arbitrarily chosen to increase by 50 percent over that of the TWT. This radius would be modified only if designing a highly efficient MDC with the resulting input beam models proved difficult.

Multistage Depressed Collector

The MDC designs were optimized for the high-power mode by using, primarily, the beam models resulting from saturated operation at midband. However, several additional requirements were imposed:

(1) The design had to be able to handle some larger injection angles, which were expected to be caused in the actual TWT by thermal velocity and other effects that were ignored in the computer model.

(2) The design had to be able to handle the increased spent-beam velocity spread that was expected during operation at the upper-band edge.

(3) The design had to work well in the low-power mode, with acceptably low levels of backstreaming to the TWT body. The cases that were used to produce each MDC design are shown in table III. The effect of larger injection angles was investigated by using a beam model in which the magnitude of all the injection angles was increased by a factor of 1.5. In the case of the first MDC design, allowance for the slow electrons expected at 64 GHz was limited to analysis of MDC performance with reduced depression on the least depressed electrode, V_{e1}, because the TWT analysis at 64 GHz had not been completed when the collector was being designed. In the case of the second MDC, a high level of MDC performance at the upper-band edge was verified by direct analysis. Low-

mode operation of the TWT system was de-emphasized. Performance optimization was limited to a parametric study, at midband frequency, with the MDC operating voltages.

The analysis of the effect of secondary-electron emission on MDC performance was limited to that of low energy secondaries. "Electrons" of 10 eV were injected back along the lines of incidence of the primary charges, and the attendant efficiency reductions were calculated. A secondary-electron-emission yield of 0.6 was assumed as a typical value for the machined isotropic-graphite-electrode surfaces of the experimental collectors (ref. 9).

TABLE IV.—COMPUTED RF PERFORMANCE OF HAC TWT MODEL 961HA

TWT parameter	High mode		Low mode	
	Frequency, GHz		Frequency, GHz	
	61.5	64.0	61.5	64.0
Output power, W	100.7	91.2	46.1	28.2
RF efficiency, percent	6.99	6.33	5.31	3.25
Gain, dB	54.2	49.8	42.8	34.7
Circuit and window losses, W	22.9	19.1	10.5	7.3
Intercepted power, W	7.1	6.6	0	0

Analytical Results

Traveling-Wave Tube

The values selected from the parametric study for the beam-to-tunnel radius ratio b/a at the RF input were 0.54 and 0.41 for the high and low modes, respectively. These values resulted in minimum beam interception at saturation for the midband frequency, 61.5 GHz. At this frequency, saturation was obtained with input powers of −4 dBm (0.4 mW) for the high mode and +4 dBm (2.5 mW) for the low mode. At 64.0 GHz, input powers of 0 dBm (1.0 mW) for the high mode and +10 dBm (10.0 mW) for the low mode produced saturation.

The computed RF performance of the TWT is shown in table IV. For the high mode, the computed RF output power exceeds the nominal 75-W level by a significant margin. Consequently, even with higher than computed beam interception and RF circuit losses in the experimental TWT's, it should be readily possible to meet the minimum requirement. For the low (30-W) mode, however, the design is marginal at best.

The total RF losses include an estimated 4.5-percent TWT window loss in the RF output power (ref. 6). The computed circuit efficiencies of 81 to 83 percent significantly exceed the estimated values of 70 to 75 percent in reference 6.

At midband the ring outer radii trajectories between the RF input and RF output are shown in figures 1 and 2. The computed spent-beam energy distributions at the RF output of the TWT are shown in figures 3 and 4 for the high and low modes, respectively. The slowest electrons are produced when the TWT is operated at the upper-band edge, in agreement with the one-dimensional results of reference 6. Other spent-beam characteristics at the RF output are given in the next section as the SBR inputs.

Spent-Beam Refocuser

The effect of RF beam debunching in the SBR is shown in figure 5, for the high mode. At midband operation, debunching causes significant changes in the spent-beam energy distribution and serves to increase the velocity spread, an

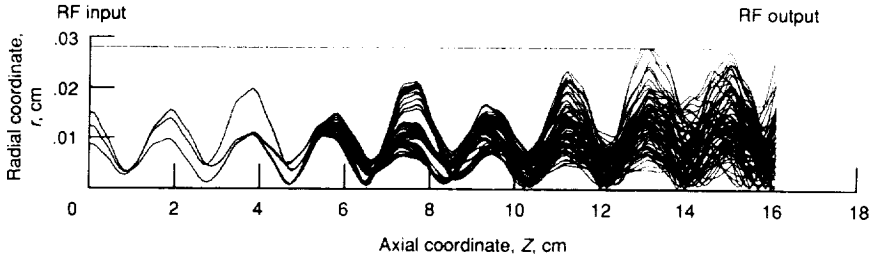

Figure 1.—Ring outer radii trajectories in TWT for saturated operation at 61.5 GHz in high mode.

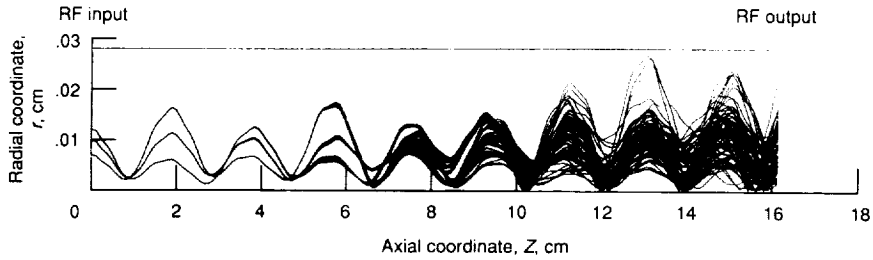

Figure 2.—Ring outer radii trajectories in TWT for saturated operation at 61.5 GHz in low mode.

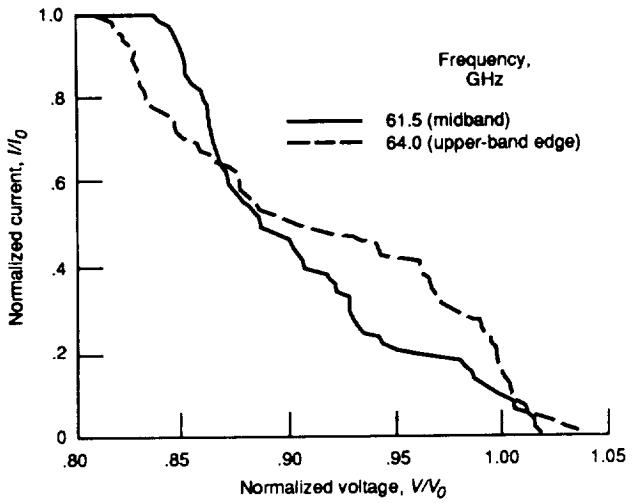

Figure 3.—Computed spent-beam energy distributions at RF output for TWT operation at saturation in high mode.

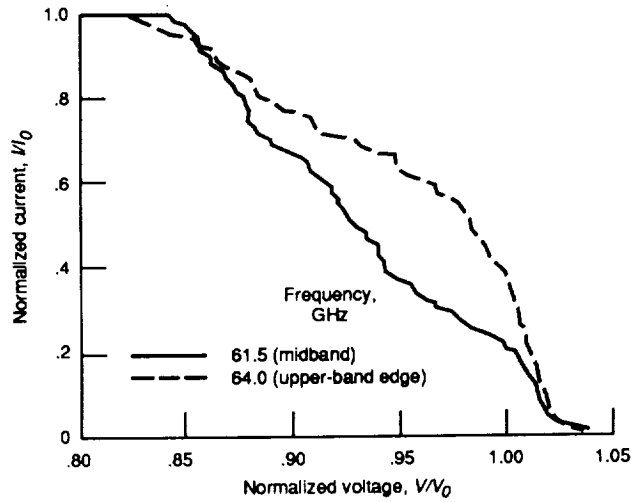

Figure 4.—Computed spent-beam energy at RF output for TWT operation at saturation in low mode.

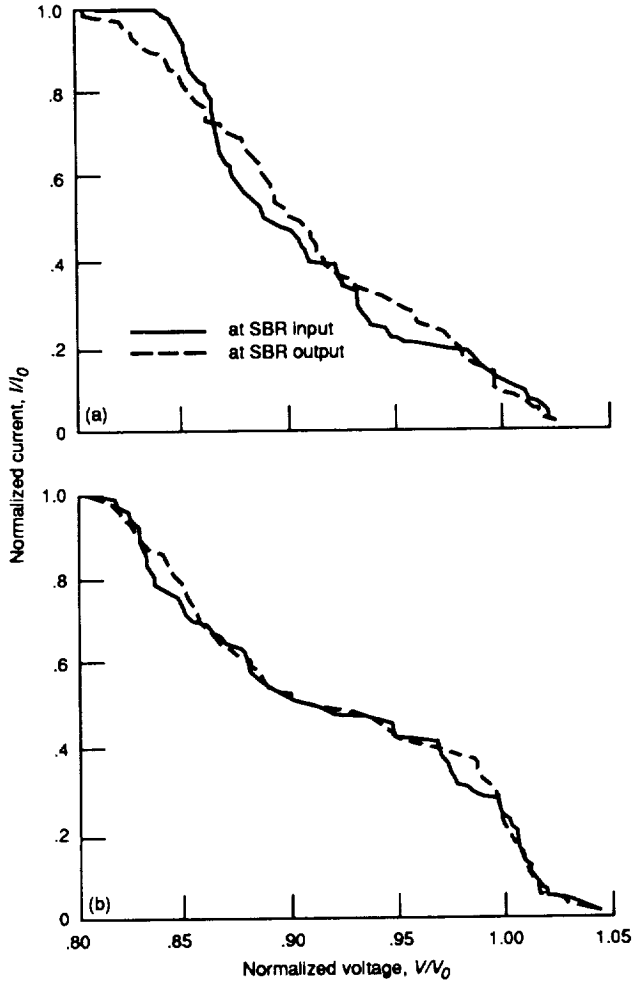

(a) At 61.5 GHz.
(b) At 64.0 GHz.

Figure 5.—Computed spent-beam energy distributions at input and output of spent-beam refocuser at saturation in high mode.

undesirable feature. At 64 GHz the effect of debunching is much smaller, with only a small change in the lowest energy, E_{min}. At the output of the SBR the minimum ring energies at midband and the upper-band edge are comparable. The low-mode results showed similar trends, but the changes in the energy distributions were smaller.

The trajectories in the last part of the RF output section and the drift tunnel are shown in figure 6 for the midband frequency of 61.5 GHz. Parts (a) and (b) of figure 6 show the ring outer radii trajectories for the unexpanded drift tunnel SBR with the high- and low-beam modes respectively, whereas parts (c) and (d) show the ring outer radii trajectories for the expanded drift tunnel SBR. In the high-beam-mode unexpanded drift tunnel case shown in figure 6(a), the beam is just barely contained within the tunnel wall; however in the low-mode case of figure 6(b), the beam edge is much closer to the axis, because of the lower current and the lower space charge. Since the coupled-cavity TWT computer model does not take into account thermal electrons, beam misalignments, and focusing magnet irregularities, the actual TWT generally experiences slightly more interception than predicted. Thus the drift tunnel should be expanded to avoid interception in the high-beam mode.

Parts (c) and (d) of figure 6 show the ring outer radii for the high- and low-beam-mode cases with an expanded drift tunnel. The expansion eliminated the problem of interception in the drift tunnel. When these parts of figure 6 are compared to parts (a) and (b), the other two effects of tunnel expansion are seen to be a small decrease in radius for most ring trajectories and a decrease in the plasma wavelength. These effects are shown more clearly in figure 7, where the average ring centroid radius trajectories for the four cases are plotted. For both high- and low-beam modes, drift tunnel expansion causes the ring radii and plasma wavelength to decrease.

To understand the physics behind these effects, it is necessary to consider the electric forces between the beam's

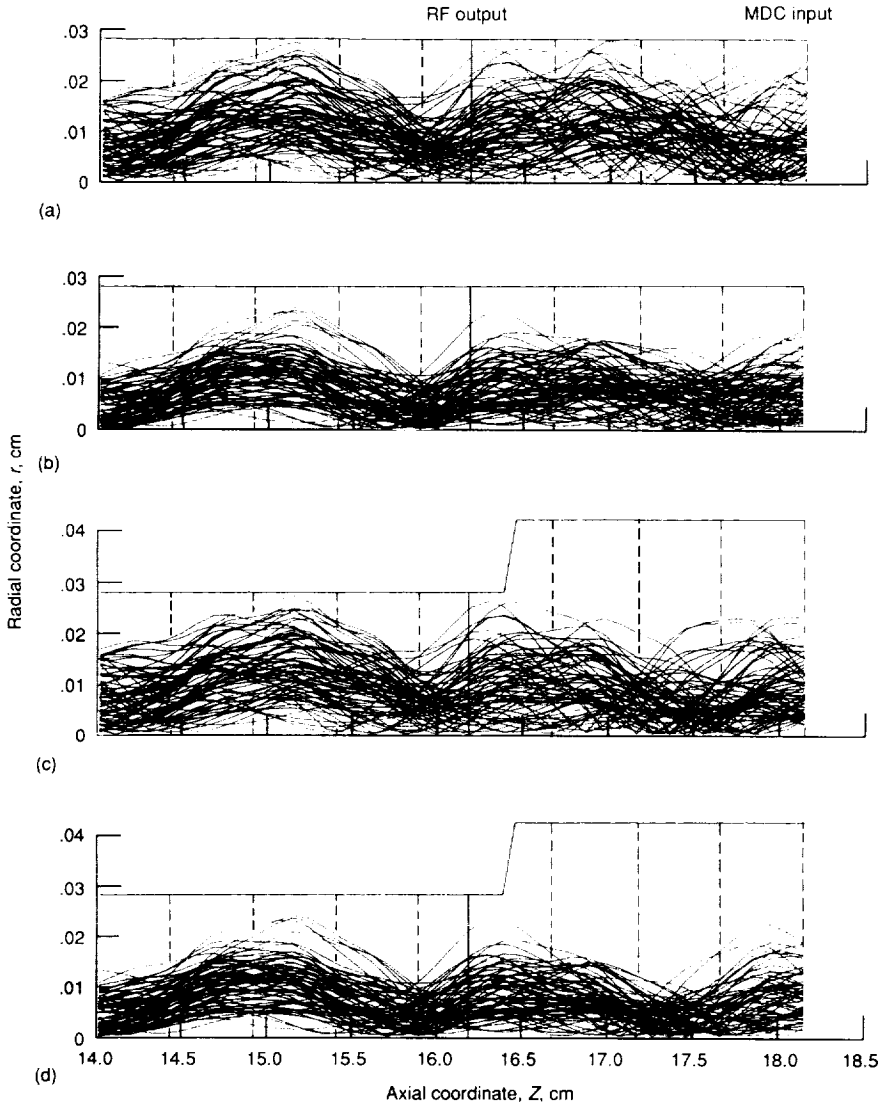

(a) High-beam mode in unexpanded drift tunnel SBR.
(b) Low-beam mode in unexpanded drift tunnel SBR.
(c) High-beam mode in expanded drift tunnel SBR.
(d) Low-beam mode in expanded drift tunnel SBR.

Figure 6.—Ring outer radii trajectories for low- and high-beam modes in expanded and unexpanded drift tunnels. Solid vertical line at 16.22 cm indicates end of RF output and beginning of SBR; MDC begins at 18.17 cm. Dashed vertical lines indicate zeroes of periodic-permanent-magnet field.

bunches and antibunches (ref. 10). The RF electric field lines, which are due to the charge density deviation from the direct current equilibrium value, point from an antibunch to a bunch. Because of the finite radius of the beam, some of the field lines will bow away from the axis. With a metal wall, more field lines bow away from the axis toward image charges on the outer side of the wall. The farther the wall is from the beam, the farther away are the image charges; and the field lines bow away less from the axis, thereby weakening the radial force and strengthening the axial force between bunch and antibunch. Thus, in an expanded drift tunnel the reduced radial space-charge forces decrease the ring trajectory radii (except at plasma wavelength peaks). The increased axial space-charge force increases the plasma frequency and decreases the plasma wavelength.

Selected beam characteristics at the input and output of the SBR are compared in tables V and VI for operating frequencies of 61.5 and 64.0 GHz, respectively. Table V compares the

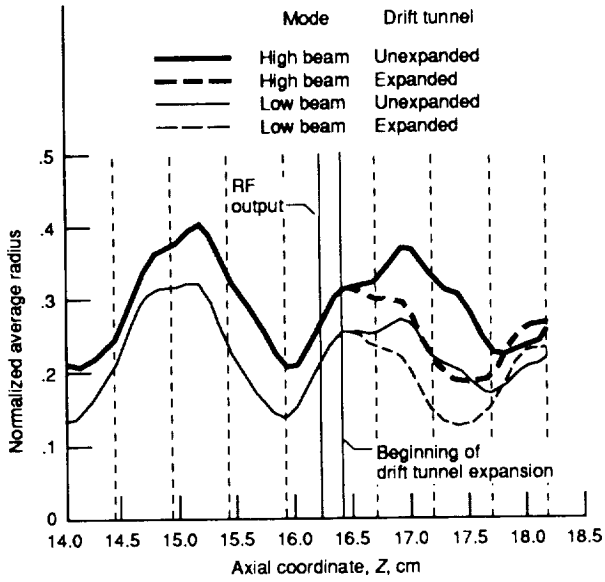

Figure 7.—Average ring centroid radius normalized to RF tunnel radius. Dashed vertical lines indicate zeroes of periodic-permanent-magnet field.

TABLE V.—BEAM CHARACTERISTICS AT INPUT AND OUTPUT OF SPENT-BEAM REFOCUSER AT SATURATION AT 61.5 GHz[a]

Beam characteristic	High mode			Low mode		
	SBR input	SBR output		SBR input	SBR output	
		Unexpanded tunnel, $R = a$, for cases 1, 2, 3	Expanded tunnel, $R = 1.5a$, for cases 5 and 6		Unexpanded tunnel, $R = a$, for case 4	Expanded tunnel, $R = 1.5a$, for case 8
Largest normalized ring radius, $(r_{max})/a$	0.78	0.71	0.45	0.54	0.54	0.35
Average normalized beam radius, r/a	0.28	0.27	0.18	0.22	0.23	0.16
Average angle of ring centroid, degrees	0.55	0.44	0.04	0.50	0.28	0.06
Standard deviation of ring angle, degrees	0.66	0.76	0.74	0.49	0.50	0.48
Fraction of negative ring angles	17/72	23/72	31/72	10/72	22/72	30/72
Range of angles, degrees	−0.9 to 1.8	−1.5 to 2.0	−2.2 to 1.4	−0.4 to 1.7	−0.7 to 1.5	−1.5 to 1.0
Minimum ring energy, E_{min}, eV	16 103	15 471	15 695	16 248	15 854	16 054

[a]Based on ring centroid.

TABLE VI.—BEAM CHARACTERISTICS AT INPUT AND OUTPUT OF SPENT-BEAM REFOCUSER WITH EXPANDED DRIFT TUNNEL AT SATURATION AT 64 GHz[a]

Beam characteristic	High mode		Low mode	
	SBR input	SBR output for case 7	SBR input	SBR output
Largest normalized ring radius, $(r_{max})/a$	0.71	0.47	0.61	0.31
Average normalized beam radius, r/a	0.23	0.18	0.21	0.13
Average angle of ring centroid, degrees	0.64	0.19	0.48	0.06
Standard deviation of ring angle, degrees	0.66	0.60	0.35	0.57
Fraction of negative ring angles	10/72	30/72	5/72	25/72
Range of angles, degrees	−0.6 to 2.4	−1.3 to 1.3	−0.3 to 1.5	−2.1 to 0.8
Minimum ring energy, E_{min}, eV	15 563	15 442	15 890	15 930

[a]Based on ring centroid.

results for a 50-percent-expanded drift tunnel to those for an unexpanded tunnel. In general, the SBR produced some beam compression and a small increase in beam disorder. These observations are consistent with those of references 8 and 11. Expanding the drift tunnel produced more beam compression and slightly larger values of the minimum energy, E_{min}, at the input to the MDC.

The angles of the ring centroids were found to be very small in all cases, both at the beginning and at the end of the SBR. For example, for the midband, high-mode, expanded tunnel SBR output, 62 of the 72 rings had centroidal angles with absolute magnitudes of less than 1°, and 13 had magnitudes of less than 0.1°. In all cases, drift through the SBR resulted in an increase in the number of negative ring angles—an undesirable effect since small, negative MDC injection angles can result in undesired backstreaming to the TWT body.

In general, all of the computed cases exhibited well-collimated beams with relatively small ranges of injection angles and energies, and of sufficiently small size to provide a good approximation to the 'point source' ideal at the input to the MDC.

Multistage Depressed Collector 1

The four-stage, axisymmetric MDC geometry, the applied potentials, the equipotential lines, and the charge trajectories are shown in figures 8 to 11 for the four beam models (table III) used to design the first MDC. The corresponding TWT–SBR–MDC power distributions, current distributions, and efficiencies are shown in tables VII to X. The very high computed collector efficiencies, of almost 95 percent in some cases, are a result of the following:

(1) A relatively small velocity spread in the beam

(2) An extremely well-collimated beam and a very favorable MDC axial electric field-to-radial space-charge field ratio (in excess of 30:1) in the lower part of the collector, which permits a very high sorting efficiency (ref. 12) because of the small amount of kinetic energy associated with radial velocity components

(3) A very favorable MDC-to-input beam size (in excess of 30:1), which makes the spent beam appear to be almost a point source at the MDC input

(4) The effective suppression of low energy secondary-electron-emission current by the MDC design

The peculiar shape of electrode 1 near its inner aperture (see fig. 8) was chosen to minimize harmful convergent lens effects in the region of the aperture. These effects are caused by a large gradient in the axial electric field in that region (see change in equipotential line spacing in fig. 8).

The beam model with increased injection angles yielded higher efficiencies than the nominal design case (table VIII compared to table VII), and operation with reduced depression on the least depressed electrode caused only a small degradation in efficiency (table IX compared to table VII). Subsequent TWT–SBR performance analyses at 64 GHz indicated that although operation at the upper-band edge resulted in the lowest value of E_{min} at the RF output, the values of E_{min} at the input to the MDC were comparable at 61.5 and 64 GHz. Consequently, reducing the depression on the first electrode to allow for operation at the upper-band edge should not be required.

The low-mode efficiencies are considerably lower than those for the high mode, because of some backstreaming current to the TWT body. Such backstreaming was found to be highly sensitive to the MDC operating voltages; perhaps an in-depth optimization study would produce significantly better results.

After the first MDC design was completed, the TWT computer program modifications that were required to model the step change in the drift tunnel radius were fully

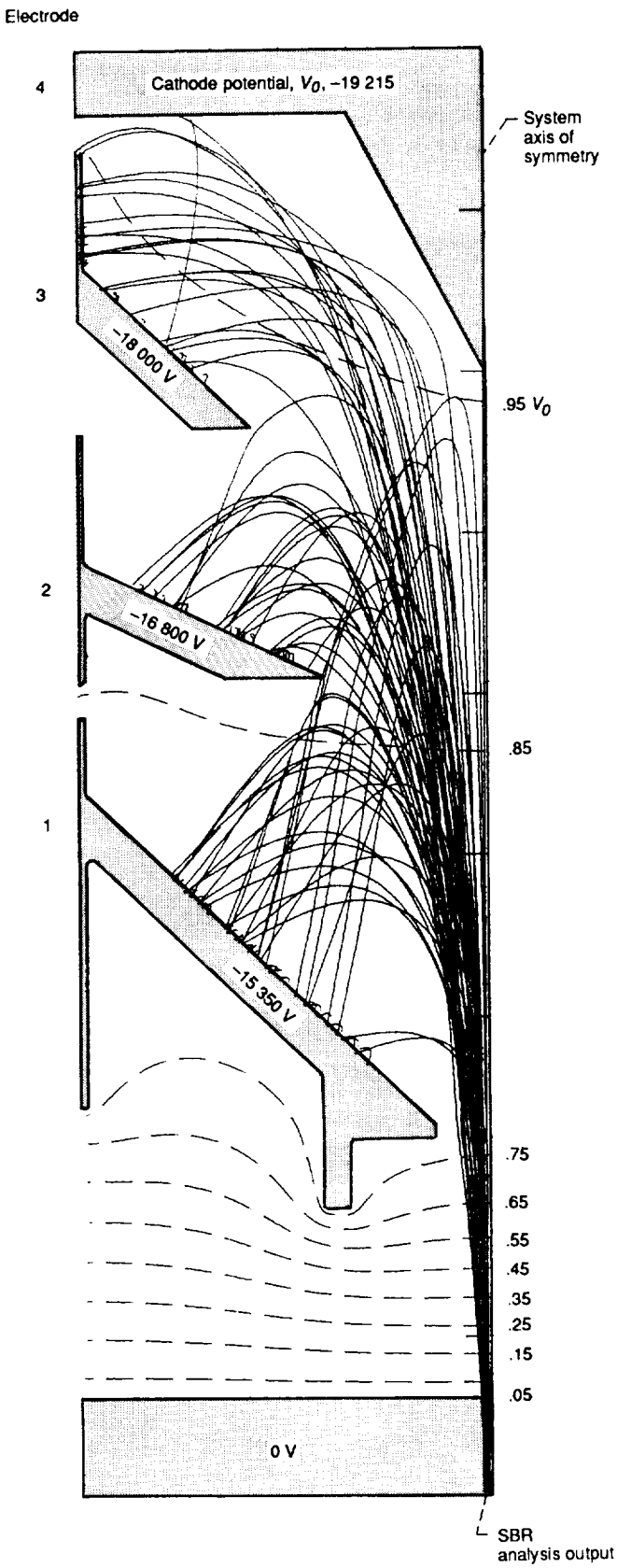

Figure 8.—Case 1: Charge trajectories in four-stage depressed collector operating at optimum voltages, with TWT operating in high mode at saturation at 61.5 GHz (first MDC design for constant radius drift tunnel SBR).

TABLE VII.—CASE 1: COMPUTED PERFORMANCE OF 961HA TWT AND FIRST MDC DESIGN, WITH TWT OPERATING IN HIGH MODE AT SATURATION AT 61.5 GHz WITH OPTIMUM MDC OPERATING VOLTAGES

[Computed trajectories shown in fig. 8.]

(a) TWT-SBR-MDC performance[a]

Electrode (fig. 3)	Voltage, kV (with respect to ground)	Current, mA	Recovered power, W	Dissipated power, W
Polepiece	0	0	0	0
1	−15.350	29.9	459.6	35.3
2	−16.800	20.7	347.3	11.8
3	−18.000	20.6	370.8	19.8
4	−19.215	.4	7.7	.5
Totals		71.6	1185.4	67.5

(b) Computed efficiency

System component	Efficiency, percent
Collector	94.6
Overall	50.8

(c) Power balance in TWT-SBR-MDC system

Component of power	Power, W
Beam interception	7.1
Total RF conversion	[b]123.6
Recovered power	1185.4
MDC dissipation	67.5
Total	1383.5

[a]Assumes an (isotropic-graphite) electrode secondary-electron-emission yield of 0.6.

[b]Includes output power, 100.7 W; window losses, 4.7 W; and circuit losses, 18.2 W.

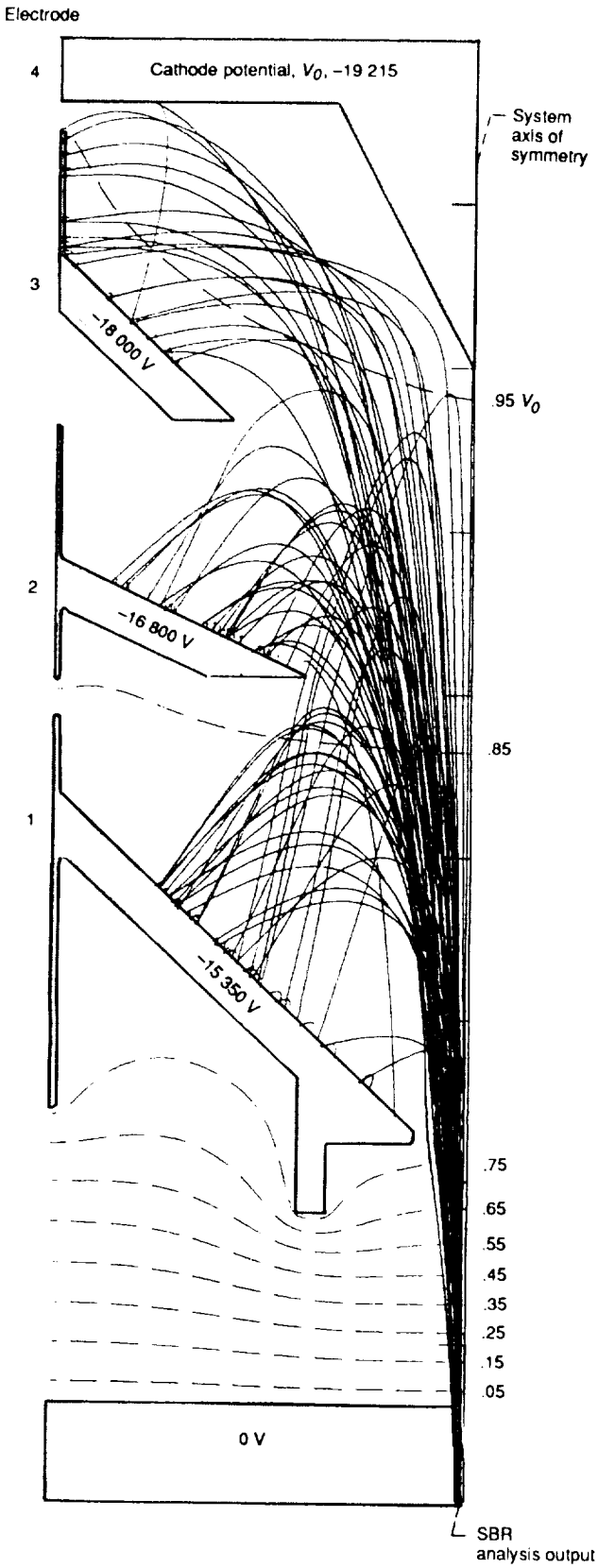

Figure 9.—Case 2: Charge trajectories in four-stage depressed collector with all input angles increased by a factor of 1.50 and with TWT operating in high mode at saturation at 61.5 GHz (first MDC design for constant radius drift tunnel SBR).

TABLE VIII.—CASE 2: COMPUTED PERFORMANCE OF 961HA TWT AND FIRST MDC DESIGN, WITH TWT OPERATING IN HIGH MODE AT SATURATION AT 61.5 GHz WITH MDC INPUT ANGLES INCREASED BY A FACTOR OF 1.50

[Computed trajectories shown in fig. 9]

(a) TWT-SBR-MDC performance[a]

Electrode (fig. 3)	Voltage, kV (with respect to ground)	Current, mA	Recovered power, W	Dissipated power, W
Polepiece	0	0	0	0
1	−15.350	27.9	428.9	31.5
2	−16.800	22.7	380.9	12.7
3	−18.000	20.6	370.8	19.8
4	−19.215	.4	7.7	.5
Totals		71.6	1188.3	64.6

(c) Computed efficiency

System component	Efficiency, percent
Collector	94.8
Overall	51.6

(c) Power balance in TWT-SBR-MDC system

Component of power	Power, W
Beam interception	7.1
Total RF conversion	[b]123.6
Recovered power	1188.3
MDC dissipation	64.6
Total	1383.6

[a]Assumes an (isotropic-graphite) electrode secondary-electron-emission yield of 0.6.

[b]Includes output power, 100.7 W; window losses, 4.7 W; and circuit losses, 18.2 W.

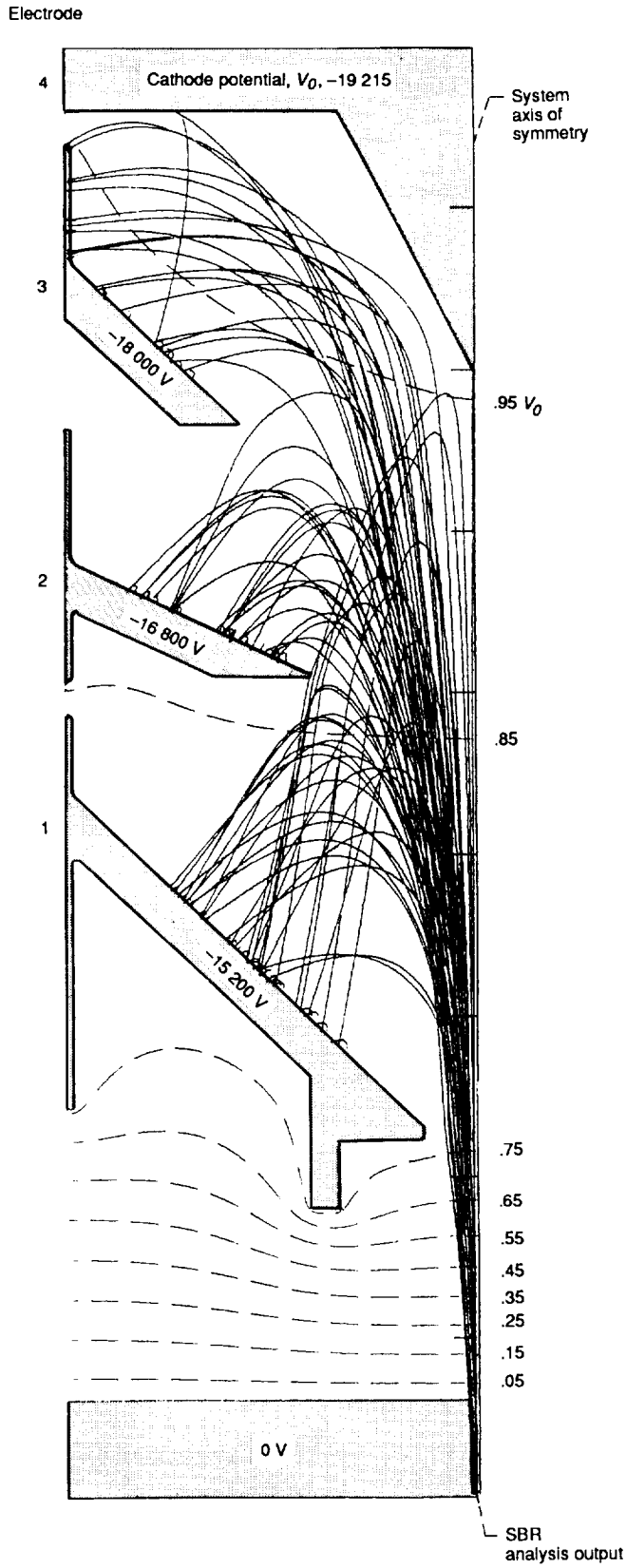

Figure 10.—Case 3: Charge trajectories in four-stage depressed collector operating with reduced depression of electrode 1 and with TWT operating in high mode at saturation at 61.5 GHz (first MDC design for constant radius drift tunnel SBR).

TABLE IX.—CASE 3: COMPUTED PERFORMANCE OF 961HA TWT AND FIRST MDC DESIGN, WITH TWT OPERATING IN HIGH MODE AT SATURATION AT 61.5 GHz AND REDUCED V_{e1}

[Computed trajectories shown in fig. 10.]

(a) TWT-SBR-MDC performance[a]

Electrode (fig. 3)	Voltage, kV (with respect to ground)	Current, mA	Recovered power, W	Dissipated power, W
Polepiece	0	0	0	0
1	−15.200	29.9	455.1	39.8
2	−16.800	20.7	347.3	11.8
3	−18.000	20.6	370.8	19.8
4	−19.215	.4	7.7	.5
Totals		71.6	1180.9	72.0

(b) Computed efficiency

System component	Efficiency, percent
Collector	94.3
Overall	49.7

(c) Power balance in TWT-SBR-MDC system

Component of power	Power, W
Beam interception	7.1
Total RF conversion	[b]123.6
Recovered power	1180.9
MDC dissipation	72.0
Total	1383.6

[a]Assumes an (isotropic-graphite) electrode secondary-electron-emission yield of 0.6.

[b]Includes output power, 100.7 W; window losses, 4.7 W; and circuit losses, 18.2 W.

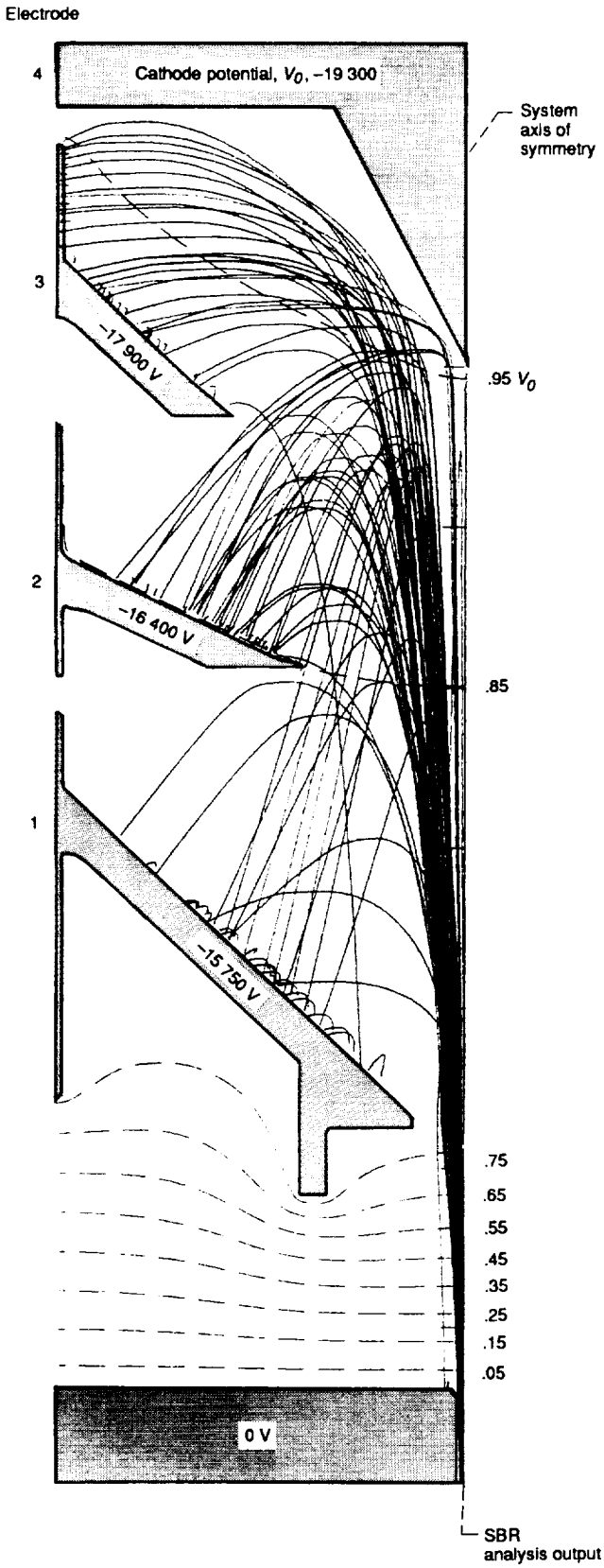

Figure 11.—Case 4: Charge trajectories in four-stage depressed collector operating at optimum voltages, with TWT operating in low mode at saturation at 61.5 GHz (first MDC design for constant radius drift tunnel SBR).

TABLE X.—CASE 4: COMPUTED PERFORMANCE OF 961HA TWT AND FIRST MDC DESIGN, WITH TWT OPERATING IN LOW MODE AT SATURATION AT 61.5 GHz WITH OPTIMUM MDC OPERATING VOLTAGES

[Computed trajectories shown in fig. 11.]

(a) TWT-SBR-MDC performance[a]

Electrode (fig. 3)	Voltage, kV (with respect to ground)	Current, mA	Recovered power, W	Dissipated power, W
Polepiece	0	0.6	0	11.0
1	−15.750	12.2	192.9	13.0
2	−16.400	16.2	266.5	22.4
3	−17.900	15.9	284.2	21.8
4	−19.300	0	0	0
Totals		45.0	743.6	68.3

(b) Computed efficiency

System component	Efficiency, percent
Collector	91.6
Overall	38.7

(c) Power balance in TWT-SBR-MDC system

Component of power	Power, W
Beam interception	0
Total RF conversion	[b]56.6
Recovered power	743.6
MDC dissipation	68.3
Total	868.5

[a]Assumes an (isotropic-graphite) electrode secondary-electron-emission yield of 0.6.

[b]Includes output power, 46.1 W; window losses, 2.2 W; and circuit losses, 8.3 W.

implemented, and the TWT analysis was extended to the upper-band edge. The performance of the first MDC design, with the resulting new high-mode beam models (table III, cases 5 to 7), was evaluated. The results were the following:

Frequency, GHz	Efficiency, percent	
	Collector	Overall
61.5	93.6	47.9
[a]61.5	94.6	50.8
64	94.4	48.6

[a]Angles increased 1.5 times.

The first MDC performed well at 64 GHz and with the larger injection angles, but it suffered a slight efficiency loss for the nominal 61.5 GHz case, because of some backstreaming current to the TWT. Therefore, an MDC design modification for the second TWT was indicated.

Multistage Depressed Collector 2

The design of the second MDC is very similar to that of the first one, with only relatively small changes in the shapes of electrodes 2 and 3. Basically, material was added to the top surfaces of the inwardly extending portions of these electrodes to make the electrodes thicker and the apertures slightly smaller. Since the vertical portions of the electrodes (insulator attachment points) were left unchanged, no changes were required in the passive electrode support structure designed by Hughes Aircraft for the first collector.

The MDC geometry, the applied potentials, the equipotential lines, and the charge trajectories are shown in figures 12 to 15 for the last four cases described in table III. The corresponding TWT–SBR–MDC power distributions, current distributions, and efficiencies are shown in tables XI to XIV. The high-mode collector efficiencies of 94 to 95 percent and the overall efficiencies of nearly 50 percent are comparable to those of the first MDC design. The efficiencies for the low mode, however, are significantly higher because of a substantially reduced level of backstreaming current to the TWT body.

The 94- to 95-percent collector efficiencies imply sorting efficiencies of nearly 99 percent. The second MDC design provides very effective suppression of low energy secondaries, with backstreaming current coming only from very small areas near the inner apertures (see, e.g., fig. 13). The resulting degradation in collector efficiency is less than 0.5 percent for the worst case (64 GHz).

As discussed above, the TWT computer analysis almost certainly underestimates the actual TWT RF-circuit and beam-interception losses; therefore, the computed overall efficiencies of about 50 percent are overly optimistic. To evaluate the effect of larger, fixed TWT losses, the overall efficiencies were recomputed with the following assumed values (based on ref. 6) for the fixed TWT losses:

(1) Intercepted power, 2 percent of the direct current beam power I_0V_0

(2) Effective circuit efficiencies, 80 and 75 percent at 61.5 and 64.0 GHz, respectively

The results for the second MDC design are shown below.

TWT operating condition	Frequency, GHz	Overall efficiency	
		With computed power losses	With realistic power losses
High mode	61.5	51.0	44.8
High mode with increased angles	61.5	50.9	44.7
High mode	64	48.6	38.2
Low mode	61.5	46.4	38.6

The efficiency degradation, which is very substantial, results from the combined effect of higher fixed losses and reduced levels of RF output power. A further reduction can be expected from higher-than-computed secondary-electron-emission losses in the MDC, because the computation neglected the effects of energetic secondaries. Nevertheless, reaching the design goal of 40-percent overall efficiency at midband frequency appears feasible.

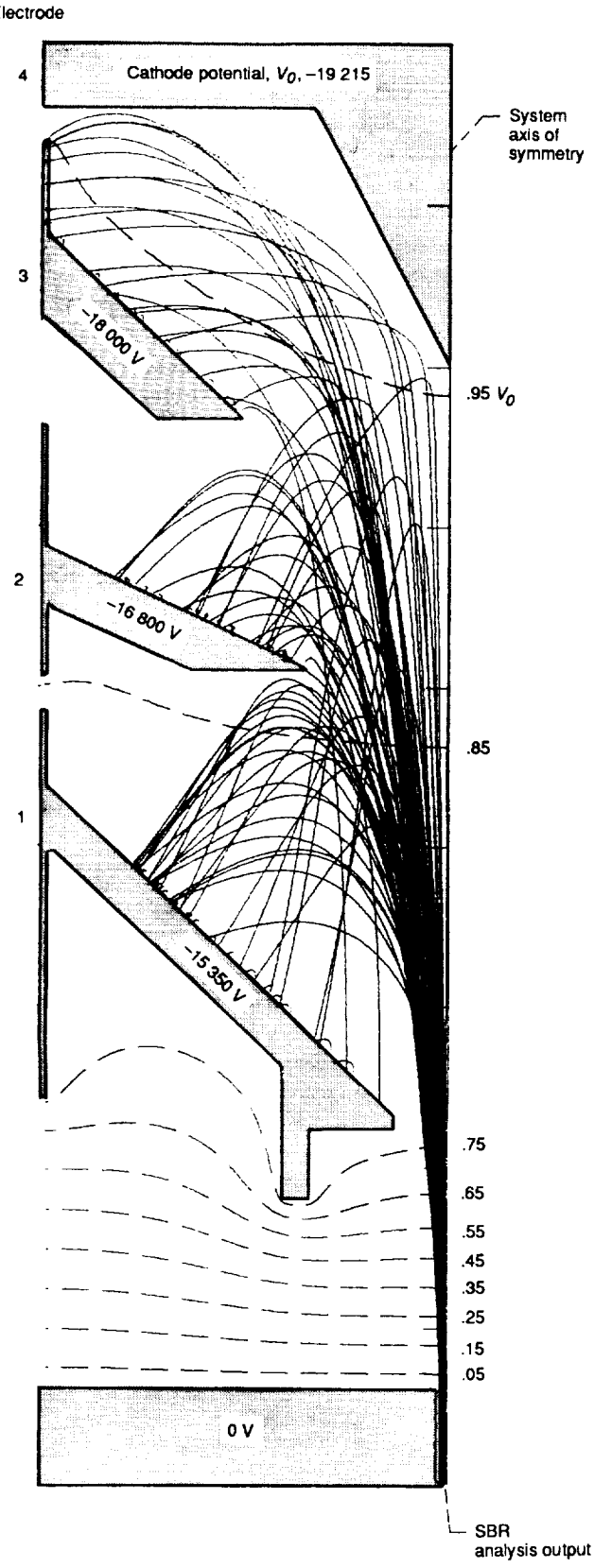

Figure 12.—Case 5: Charge trajectories in four-stage depressed collector operating at optimum voltages, with TWT operating in high mode at saturation at 61.5 GHz (second MDC design for expanded radius drift tunnel SBR).

TABLE XI.—CASE 5: COMPUTED PERFORMANCE OF 961HA TWT AND SECOND MDC DESIGN, WITH TWT OPERATING IN HIGH MODE AT SATURATION AT 61.5 GHz WITH OPTIMUM MDC OPERATING VOLTAGES

[Computed trajectories shown in fig. 12.]

(a) TWT-SBR-MDC performance[a]

Electrode (fig. 3)	Voltage, kV (with respect to ground)	Current, mA	Recovered power, W	Dissipated power, W
Polepiece	0	0	0	0
1	−15.350	28.5	438.1	32.0
2	−16.800	22.7	380.9	14.6
3	−18.000	20.4	367.2	20.0
4	−19.215	0	0	0
Totals		71.6	1186.2	66.6

(b) Computed efficiency

System component	Efficiency, percent
Collector	94.7
Overall	51.0

(c) Power balance in TWT-SBR-MDC system

Component of power	Power, W
Beam interception	7.1
Total RF conversion	[b]123.6
Recovered power	1186.2
MDC dissipation	66.6
Total	1383.5

[a]Assumes an (isotropic-graphite) electrode secondary-electron-emission yield of 0.6.

[b]Includes output power, 100.7 W; window losses, 4.7 W; and circuit losses, 18.2 W.

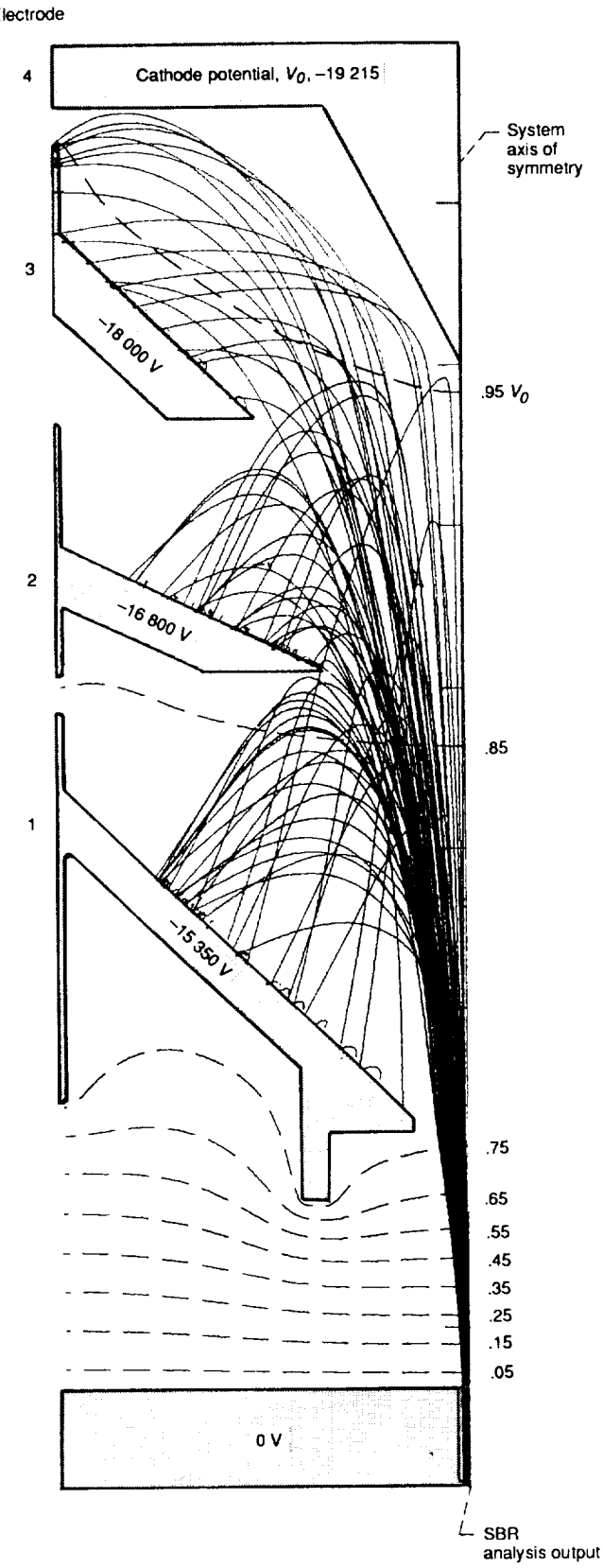

Figure 13.—Case 6: Charge trajectories in four-stage depressed collector with all input angles increased by a factor of 1.50 and with TWT operating in high mode at saturation at 61.5 GHz (second MDC design for expanded radius drift tunnel SBR).

TABLE XII.—CASE 6: COMPUTED PERFORMANCE OF 961HA TWT AND SECOND MDC DESIGN, WITH TWT OPERATING IN HIGH MODE AT SATURATION AT 61.5 GHz WITH MDC INPUT ANGLES INCREASED BY A FACTOR OF 1.50

[Computed trajectories shown in fig. 13.]

(a) TWT–SBR–MDC performance[a]

Electrode (fig. 3)	Voltage, kV (with respect to ground)	Current, mA	Recovered power, W	Dissipated power, W
Polepiece	0	0	0	0
1	−15.350	28.5	438.1	32.8
2	−16.800	23.1	387.6	14.6
3	−18.000	20.0	360.0	19.8
4	−19.215	0	0	0
Totals		71.6	1185.7	67.1

(c) Computed efficiency

System component	Efficiency, percent
Collector	94.6
Overall	50.9

(c) Power balance in TWT–SBR–MDC system

Component of power	Power, W
Beam interception	7.1
Total RF conversion	[b]123.6
Recovered power	1185.7
MDC dissipation	67.1
Total	1383.5

[a]Assumes an (isotropic-graphite) electrode secondary-electron-emission yield of 0.6.

[b]Includes output power, 100.7 W; window losses, 4.7 W; and circuit losses, 18.2 W.

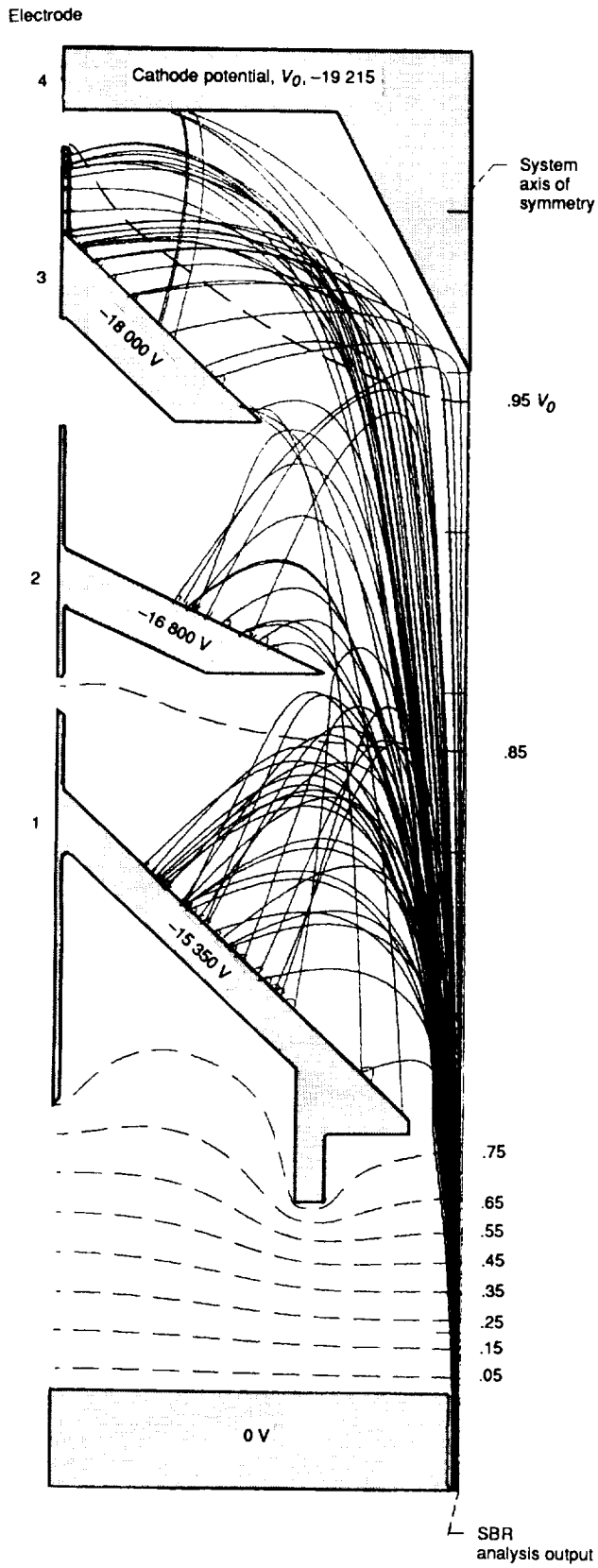

Figure 14.—Case 7: Charge trajectories in four-stage depressed collector with TWT operating in high mode at saturation at 64 GHz (second MDC design for expanded radius drift tunnel SBR).

TABLE XIII.—CASE 7: COMPUTED PERFORMANCE OF 961HA TWT AND SECOND MDC DESIGN, WITH TWT OPERATING IN HIGH MODE AT SATURATION AT 64 GHz

[Computed trajectories shown in fig. 14.]

(a) TWT-SBR-MDC performance[a]

Electrode (fig. 3)	Voltage, kV (with respect to ground)	Current, mA	Recovered power, W	Dissipated power, W
Polepiece	0	0	0	0
1	−15.350	30.0	460.2	27.5
2	−16.800	12.8	215.7	9.4
3	−18.000	27.6	496.8	32.0
4	−19.215	1.2	23.1	1.9
Totals		71.6	1195.7	70.8

(b) Computed efficiency

System component	Efficiency, percent
Collector	94.4
Overall	48.6

(c) Power balance in TWT-SBR-MDC system

Component of power	Power, W
Beam interception	6.6
Total RF conversion	[b]110.4
Recovered power	1195.7
MDC dissipation	70.8
Total	1383.5

[a]Assumes an (isotropic-graphite) electrode secondary-electron-emission yield of 0.6.

[b]Includes output power, 91.2 W; window losses, 4.3 W; and circuit losses, 14.8 W.

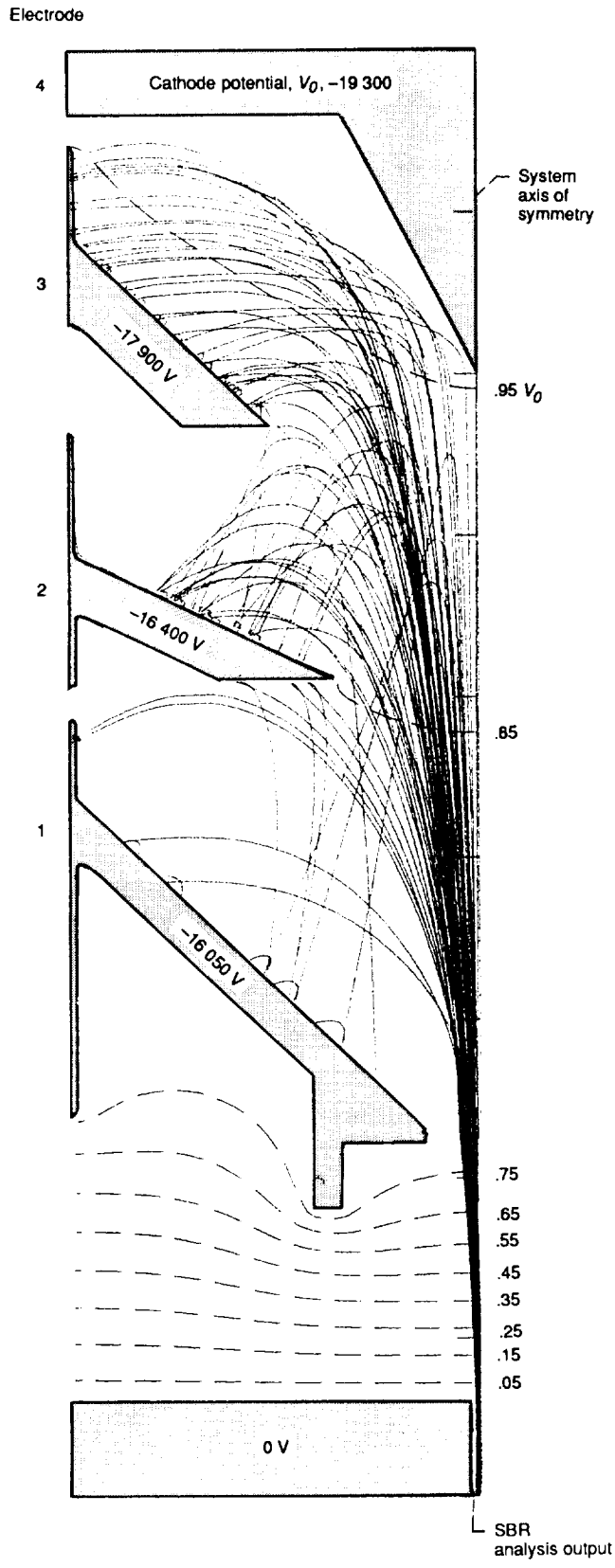

Figure 15.—Case 8: Charge trajectories in four-stage depressed collector operating at optimum voltages and with TWT operating in low mode at saturation at 61.5 GHz (second MDC design for expanded radius drift tunnel SBR).

TABLE XIV.—CASE 8: COMPUTED PERFORMANCE OF 961HA TWT AND SECOND MDC DESIGN, WITH TWT OPERATING IN LOW MODE AT SATURATION AT 61.5 GHz WITH OPTIMUM MDC OPERATING VOLTAGES

[Computed trajectories shown in fig. 15.]

(a) TWT-SBR-MDC performance[a]

Electrode (fig. 3)	Voltage, kV (with respect to ground)	Current, mA	Recovered power, W	Dissipated power, W
Polepiece	0	0	0	0
1	−16.05	5.9	94.3	4.2
2	−16.40	17.0	278.8	15.6
3	−17.90	22.1	396.0	23.0
4	−19.30	0	0	0
Totals		45.0	769.1	42.7

(b) Computed efficiency

System component	Efficiency, percent
Collector	94.7
Overall	46.4

(c) Power balance in TWT-SBR-MDC system

Component of power	Power, W
Beam interception	0
Total RF conversion	[b]56.6
Recovered power	769.1
MDC dissipation	42.7
Total	868.5

[a]Assumes an (isotropic-graphite) electrode secondary-electron-emission yield of 0.6.

[b]Includes output power, 46.1 W; window losses, 2.2 W; and circuit losses, 8.3 W.

Concluding Remarks

A computational design procedure for coupled-cavity traveling-wave tubes (TWT's) equipped with spent-beam refocusers (SBR's) and multistage depressed collectors (MDC's) has been described. It was used to design two small, highly efficient MDC's for a 59- to 64-GHz TWT. The design technique closely parallels the verified procedures devised for helical TWT's and klystrons.

In the analysis of the procedure, a coupled-cavity TWT computer model was used to determine electron ring trajectories through a TWT and SBR, for high- and low-beam power modes at the mid- and upper-band frequencies. From the results obtained for both an unexpanded and a 50-percent-expanded tunnel radius in the SBR, the main effect of the tunnel expansion was found to be compression of the beam. This compression was beneficial because it eliminated the problem of beam interception in the SBR. However, for this particular TWT, the tunnel expansion had only a relatively small effect on the MDC design and, consequently, only a very minor change in MDC efficiency. Such may not be the case for TWT's that produce considerably tighter bunches at the RF output.

The MDC designs were optimized for the high-power mode by using, primarily, the beam output from the SBR at saturated operation and midband frequency. Very high collector efficiencies of over 94 percent were computed. The relatively small velocity spread in the beam, a large MDC-to-input beam size, and the effective suppression of low energy secondary-electron-emission current all combined to make this possible.

The high computed collector efficiencies produced overall efficiencies of about 50 percent for both MDC designs at high-power-mode operation. Because the TWT analysis underestimates actual RF-circuit and beam-interception losses, the experimental overall efficiencies are expected to be closer to 40 percent.

Lewis Research Center
National Aeronautics and Space Administration
Cleveland, Ohio, May 8, 1990

References

1. Dayton, J.A. Jr., et al.: Experimental Verification of a Computational Procedure for the Design of TWT-Refocuser-MDC Systems. IEEE Trans. Electron Devices, vol. ED-28, no. 12, Dec. 1981, pp. 1480-1489.
2. McCune, E.W.: UHF-TV Klystron Multistage Depressed Collector Development Program. NASA CR-182190, 1988.
3. Connolly, D.J. and O'Malley, T.A.: Computer Program for Analysis of Coupled-Cavity Traveling-Wave Tubes. NASA TN D-8492, 1977.
4. Wilson, J.D.: Revised NASA Axially Symmetric Ring Model for Coupled-Cavity Traveling-Wave Tubes. NASA TP-2675, 1987.
5. Herrmannsfeldt, W.B.: Electron Trajectory Program. SLAC-166, Stanford Linear Accelerator Center, Sept. 1973.
6. Rousseau, A.L.; Tammaru, I; and Vassari, J.P.: Development of a 75 Watt 60 GHz Traveling-Wave Tube for Intersatellite Communications. NASA CR-182135, 1988.
7. Gilmour, A.S., Jr.: Microwave Tubes. Artech House, Inc., Norwood, MA, 1986, p. 327.
8. Ramins, P., et al.: A Re-examination of Spent Beam Refocusing for High-Efficiency Helix TWT's and Small MDC's. IEEE Trans. Electron Devices, vol. 35, no. 4, Apr. 1988, pp. 539-548.
9. Curren, A.N. and Jensen, K.A.: Secondary Electron Emission Characteristics of Ion-Textured Copper and High-Purity Isotropic Graphite Surfaces. NASA TP-2342, 1984.
10. Gewartowski, J.W. And Watson, J.A.: Principles of Electron Tubes, Including Grid-Controlled Tubes, Microwave Tubes, and Gas Tubes. D. Van Nostrand Co., 1965, pp. 329-331.
11. True, R.: Emittance and the Design of Beam Formation, Transport, and Collection Systems in Periodically Focussed TWT's. IEEE Trans. Electron Devices, vol. ED-34, no. 2, Feb. 1987, pp. 473-485.
12. Kosmahl, H.G.: Modern Multistage Depressed Collectors—A Review. Proceedings IEEE, vol. 70, no. 11, Nov. 1982, pp. 1325-1334.

NASA
National Aeronautics and Space Administration

Report Documentation Page

1. Report No.	2. Government Accession No.	3. Recipient's Catalog No.
NASA TP-3039		

4. Title and Subtitle	5. Report Date
Spent-Beam Refocusing Analysis and Multistage Depressed Collector Design for a 75-W, 59- to 64-GHz Coupled-Cavity Traveling-Wave Tube	August 1990
	6. Performing Organization Code

7. Author(s)	8. Performing Organization Report No.
Jeffrey D. Wilson, Peter Ramins, and Dale A. Force	E-5455
	10. Work Unit No. 506-44-2B

9. Performing Organization Name and Address	11. Contract or Grant No.
National Aeronautics and Space Administration Lewis Research Center Cleveland, Ohio 44135-3191	
	13. Type of Report and Period Covered Technical Paper

12. Sponsoring Agency Name and Address	14. Sponsoring Agency Code
National Aeronautics and Space Administration Washington, D.C. 20546-0001	

15. Supplementary Notes

16. Abstract

A computational design technique for coupled-cavity traveling-wave tubes (TWT's) equipped with spent-beam refocusers (SBR's) and multistage depressed collectors (MDC's) is described. A large-signal multidimensional computer program was used to analyze the TWT-SBR performance and to generate the spent-beam models used for MDC design. The results of a design involving a 75-W, 59 to 64 GHz TWT are presented. The SBR and MDC designs are shown, and the computed TWT, SBR, and MDC performances are described. Collector efficiencies in excess of 94 percent led to projected overall TWT efficiencies in the 40-percent range.

17. Key Words (Suggested by Author(s))	18. Distribution Statement
Multistage depressed collector Coupled-cavity Traveling-wave tube	Unclassified – Unlimited Subject Category 33

19. Security Classif. (of this report)	20. Security Classif. (of this page)	21. No. of pages	22. Price*
Unclassified	Unclassified	22	A03

NASA FORM 1626 OCT 86

*For sale by the National Technical Information Service, Springfield, Virginia 22161

NASA-Langley, 1990

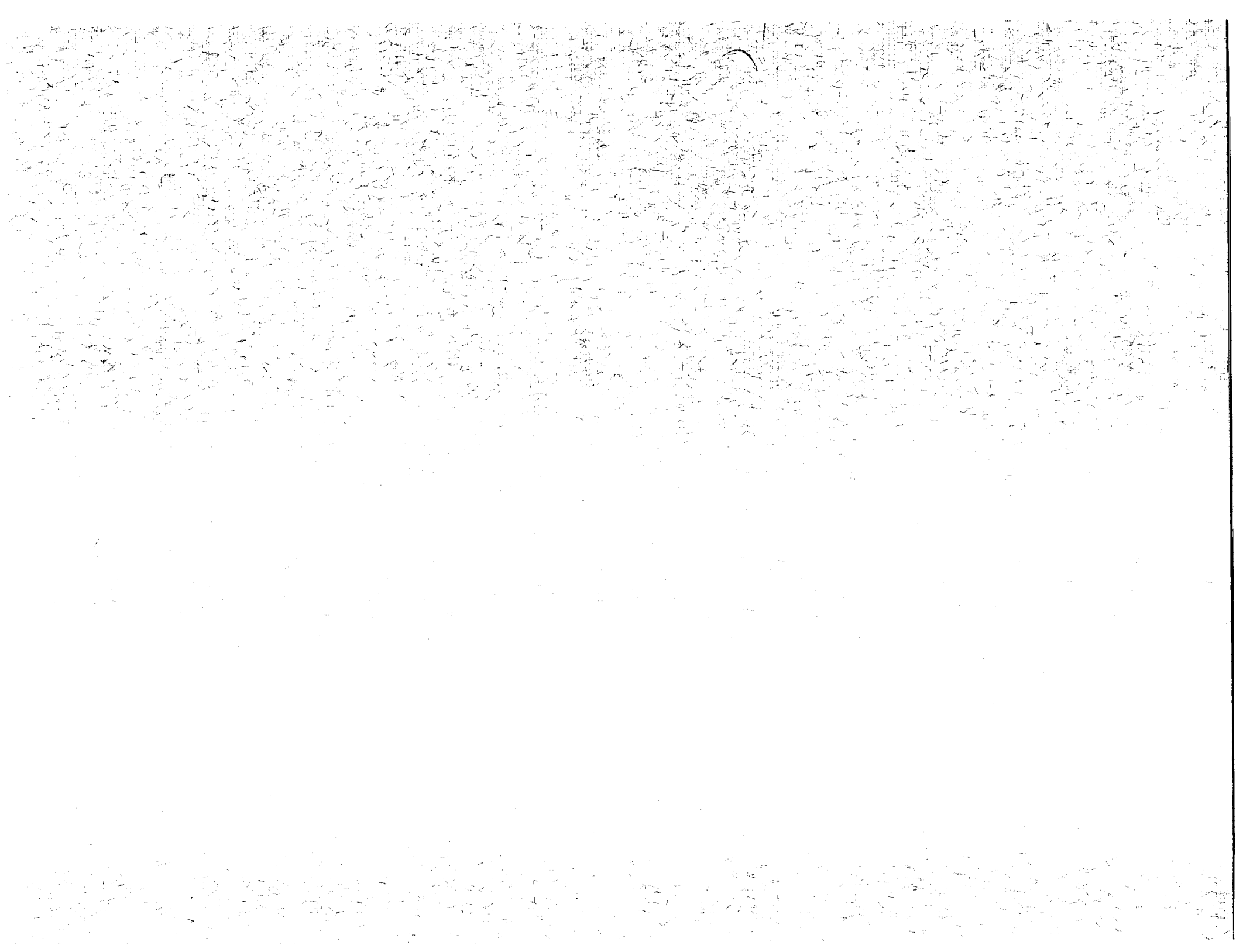

National Aeronautics and
Space Administration
Code NTT-4

Washington, D.C.
20546-0001

Official Business
Penalty for Private Use, $300

BULK RATE
POSTAGE & FEES PAID
NASA
Permit No. G-27

NASA

POSTMASTER: If Undeliverable (Section 158
Postal Manual) Do Not Return